AGU ADVANCING EARTH AND SPACE SCIENCES

AGU Advances

RESEARCH ARTICLE
10.1029/2024AV001318

Anthropogenic Aerosols Have Significantly Weakened the Regional Summertime Circulation in the Northern Hemisphere During the Satellite Era

Joonsuk M. Kang[1], **Tiffany A. Shaw**[1], **and Lantao Sun**[2]

[1]Department of the Geophysical Sciences, The University of Chicago, Chicago, IL, USA, [2]Department of Atmospheric Sciences, Colorado State University, Fort Collins, CO, USA

Peer Review The peer review history for this article is available as a PDF in the Supporting Information.

Key Points:

- Aerosol forcing has significantly weakened the regional summertime circulation in the Northern Hemisphere
- Aerosol-induced shortwave radiation trends are largest over Eurasia and result in energy export to the ocean via the stationary circulation
- Aerosol-induced energy export from land weakens the storm track over the ocean, particularly in the Pacific

Supporting Information:

Supporting Information may be found in the online version of this article.

Correspondence to:

J. M. Kang,
jmkang@uchicago.edu

Citation:

Kang, J. M., Shaw, T. A., & Sun, L. (2024). Anthropogenic aerosols have significantly weakened the regional summertime circulation in the Northern Hemisphere during the satellite era. *AGU Advances*, *5*, e2024AV001318. https://doi.org/10.1029/2024AV001318

Received 13 MAY 2024
Accepted 15 OCT 2024

Author Contributions:

Conceptualization: Joonsuk M. Kang, Tiffany A. Shaw, Lantao Sun
Data curation: Joonsuk M. Kang
Formal analysis: Joonsuk M. Kang
Funding acquisition: Joonsuk M. Kang, Tiffany A. Shaw, Lantao Sun
Investigation: Joonsuk M. Kang, Tiffany A. Shaw, Lantao Sun
Methodology: Joonsuk M. Kang, Tiffany A. Shaw
Project administration: Joonsuk M. Kang, Tiffany A. Shaw, Lantao Sun
Resources: Tiffany A. Shaw

Abstract Reanalysis data show a significant weakening of summertime circulation in the Northern Hemisphere (NH) midlatitudes in the satellite era with implications for surface weather extremes. Recent work showed the weakening is not significantly affected by changes in the Arctic, but did not examine the role of different anthropogenic forcings such as aerosols. Here we use the Detection and Attribution Model Intercomparison Project (DAMIP) simulations to quantify the impact of anthropogenic aerosol and greenhouse gas forcing. The DAMIP simulations show aerosols and greenhouse gases contribute equally to zonal-mean circulation weakening. Regionally, aerosol dominates the Pacific storm track weakening whereas greenhouse gas dominates in the Atlantic. Using a regional energetic framework, we show why the impact of aerosol is the largest in the Pacific. Reduced sulfate aerosol emissions over Eurasia and North America increase (clear-sky) surface shortwave radiation and turbulent fluxes. This enhances land-to-ocean energy contrast and energy transport via stationary circulations to the ocean. Consequently, energy converges poleward of oceanic storm tracks, demanding weaker poleward energy transport storm tracks, and the storm tracks weaken. The impact is larger over the Pacific following the larger emission decrease over Eurasia than North America. Similar yet opposite, increased aerosol emissions over South and East Asia decrease shortwave radiation and weaken land-to-ocean energy transport. This diverges energy equatorward of the Pacific storm track, further weakening it. Our results show aerosols are a dominant driver of regional circulation weakening during the NH summertime in the satellite era and a regional energetic framework explaining the underlying processes.

Plain Language Summary Over the last four decades, Northern Hemisphere summertime westerlies and weather systems have weakened. While this has important implications for weather and its extremes, how different anthropogenic forcings, such as aerosols and greenhouse gases, have impacted the weakening is currently unclear. Using coordinated climate model simulations, we show anthropogenic aerosols are as important as greenhouse gases for the weakening of the weather systems and the most important over the Pacific. Efforts to reduce aerosol emissions over North America and Europe increased the solar energy reaching the surface, whereas heightened pollution from Asia decreased the solar energy reaching the surface. As a result, energy increases at higher latitudes and decreases at lower latitudes, weakening the equator-to-pole energy (temperature) difference consistent with weaker weather systems. This effect is greater in the Pacific. Our results emphasize that how aerosol emissions will evolve in the future has important implications for regional climate change.

1. Introduction

Climatologically, the Northern Hemisphere (NH) midlatitude circulation is the weakest during summertime (Hoskins & Hodges, 2019; Shaw et al., 2018). Under anthropogenic forcing, the NH summertime circulation is projected to become weaker over the 21st century (Coumou et al., 2015; Harvey et al., 2020; O'Gorman, 2010; Shaw et al., 2018; Shaw & Voigt, 2015). Over the satellite era (1980 to present), reanalysis data show a statistically significant weakening of the zonal-mean NH summertime circulation, including storm tracks and jets (Chang et al., 2016; Chemke & Coumou, 2024; Coumou et al., 2015; Dong et al., 2022; Gertler & O'Gorman, 2019; Kang et al., 2023). The weakening of the summertime midlatitude circulation implies more persistent summertime weather (Pfleiderer et al., 2019), which could have an important influence on temperature extremes (Chang et al., 2016; Lehmann & Coumou, 2015) and local air quality (Leibensperger et al., 2008). Hence, it is essential to understand the drivers and mechanisms responsible for the weakening.

Software: Joonsuk M. Kang, Tiffany A. Shaw
Supervision: Tiffany A. Shaw, Lantao Sun
Validation: Joonsuk M. Kang, Tiffany A. Shaw, Lantao Sun
Visualization: Joonsuk M. Kang
Writing – original draft: Joonsuk M. Kang
Writing – review & editing: Joonsuk M. Kang, Tiffany A. Shaw, Lantao Sun

The weakening of the NH summertime circulation in the satellite era has been hypothesized to be related to Arctic Amplification which weakens the equator-to-pole temperature gradient (Coumou et al., 2015, 2018). However, Kang et al. (2023) used climate model simulations with nudged Arctic sea ice to show that Arctic sea ice loss and Arctic Amplification do not significantly contribute to the summertime circulation weakening in the satellite era. Instead, Kang et al. (2023) suggested anthropogenic forcing in the absence of Arctic Amplification or Arctic sea ice loss dominates the circulation weakening. Anthropogenic forcings include direct CO_2 radiative forcings (Shaw et al., 2018; Shaw & Voigt, 2015, 2016) and aerosols (Dong et al., 2022; Dong & Sutton, 2021).

Both CO_2 direct radiative and aerosol forcings directly impact the energy balance over land and thereby affect the summertime circulation. For example, Shaw et al. (2018) revealed that direct CO_2 radiative forcing over high latitude land (see Figure 1c in Shaw and Voigt (2016)) weakens the NH summertime zonal-mean storm tracks by increasing local surface turbulent fluxes and thereby weakening the equator-to-pole energy gradient. Dong et al. (2022) demonstrated that anthropogenic aerosol forcing has induced high-latitude warming and low-latitude cooling across the Eurasian continent, which through thermal wind balance leads to a weakening of the summertime Eurasian jet. Chemke and Coumou (2024) reported aerosols and greenhouse gases both contribute to weakening zonal-mean storm tracks in CESM2 (Danabasoglu et al., 2020). However, it is currently unclear how anthropogenic aerosol emissions, which occur over the land, impact the circulation downstream.

Anthropogenic aerosol can impact atmospheric circulation through aerosol-radiation and/or aerosol-cloud effects (Allen & Sherwood, 2011; Dong et al., 2022; Dow et al., 2021; Ming et al., 2011; Ming & Ramaswamy, 2009; Shen & Ming, 2018; Wang et al., 2014), mediated by ocean-atmosphere interactions (Xie et al., 2013). In the satellite era, the primary feature of aerosol emissions change is the decrease in sulfate aerosols (shortwave reflectors) over Europe and North America, and the increase over South and East Asia (Hodnebrog et al., 2024; Hoesly et al., 2018; Klimont et al., 2013; Quaas et al., 2022). The direct effects from these emission changes are spatially inhomogeneous clear-sky surface shortwave trends that are opposite to the aerosol emission trends (Diao et al., 2021; Dong et al., 2022; Schumacher et al., 2024). Previous work studied how the spatially inhomogeneous shortwave radiation changes expand and shift the annual-mean Hadley circulation (Diao et al., 2021; Wang et al., 2015), and weaken northward energy transport (Needham & Randall, 2023), and showed that they can induce different surface temperature trends over the Pacific and Atlantic oceans (Diao et al., 2021; Kang et al., 2021). However, it is currently unclear how aerosol changes impact the regional circulation during NH summertime and what the underlying mechanisms are.

In this study, our objective is to quantitatively assess the impact of anthropogenic aerosols on the recent regional weakening of the NH summertime circulation, with a particular focus on storm tracks. To achieve this, we address the following questions. (a) How do different anthropogenic forcings impact the regional summertime circulation weakening in the satellite era? Do they have the same impact on the Pacific and Atlantic storm tracks? (b) What physical mechanisms connect the regional aerosol changes over land to circulation trends during NH summertime? Is the mechanism similar to other shortwave radiation forcing, for example, the response to Arctic sea ice loss, the seasonal transition, or changes in insolation like during the mid-Holocene (Boos & Korty, 2016; Kang et al., 2023; Shaw et al., 2018; Shaw & Smith, 2022)? The questions are answered using the CMIP6 Detection and Attribution Model Intercomparison Project (DAMIP, Gillett et al., 2016) simulations and a regional energetic framework (Boos & Korty, 2016) that connects the atmospheric circulation to the shortwave radiation trends induced by regional aerosol emissions.

2. Data and Methods

2.1. Reanalysis Data Sets

We use reanalysis data sets to quantify the circulation trends in the satellite era. To account for observational uncertainty (Schmidt, 2013), we use four reanalysis data sets: CFSR/CFSv2 (Saha et al., 2010, 2014), MERRA2 (Gelaro et al., 2017; Hersbach et al., 2020), and JRA3Q (Kosaka et al., 2024), which are the latest data sets from different reanalysis centers.

The reanalysis trends from 1980 to 2020 are quantified as the slope of least-squares fit linear regression, and the statistical significance is evaluated as the 95% confidence level using a two-sided Student's *t*-test.

2.2. CMIP6 DAMIP Simulations

We use the CMIP6 DAMIP (Gillett et al., 2016) simulations to quantitatively separate the role of anthropogenic aerosols from greenhouse gas forcing on the summertime circulation trends in the satellite era. The single forcing simulations for anthropogenic aerosol (hist-aer, hereafter AER), greenhouse gas (hist-GHG, hereafter GHG), and natural forcing (hist-nat, hereafter NAT) are compared with the historical (1980–2014) and SSP245 (2015–2020) simulations (hereafter ALL for all forcing) in the CMIP6 ScenarioMIP (Eyring et al., 2016). The aerosol forcing in the AER simulation represents decreasing sulfate aerosol emissions over Europe and North America and increasing sulfate aerosols and black carbon over South and East Asia in the satellite era (Gidden et al., 2019; Hoesly et al., 2018). Further details of historical aerosol forcing in the AER simulations are introduced in Hoesly et al. (2018).

To answer the first series of questions, we use all models and realizations that have daily mean variables to quantify circulation trends across ALL, GHG, AER, and NAT simulations. For zonal and meridional winds at pressure levels, there are 35 simulations from 8 models, and for sea-level pressure (SLP), there are 43 simulations from 11 models (Table S1 in Supporting Information S1). To answer the second series of questions, we utilize 26 simulations from 5 models that have daily-mean meridional wind, temperature, geopotential, and specific humidity in AER simulations (Table S1 in Supporting Information S1). The ensemble mean is created by taking an average across all simulations. Although different models have different numbers of realizations, the results are consistent if we first average across different realizations in different models and then take the multi-model mean, as we show later. The ensemble-mean trend likely represents the forced response to individual forcings, and the ensemble spread represents both structural uncertainty and internal variability (Deser et al., 2020). As in reanalysis, the trends are calculated from 1980 to 2020 for each realization.

2.3. Summertime Circulation Metrics

We evaluate the summertime circulation trends using various metrics across reanalyses and DAMIP simulations. We specifically focus on those documented in previous work and available across a sufficient number of simulations, which are as follows.

We quantify summertime (June-July-August) storm tracks using two different metrics. First, we use vertically integrated eddy kinetic energy (hereafter EKE) defined as follows (Kang et al., 2023):

$$EKE = \frac{1}{g}\int_{p_s}^{10\text{hPa}} \frac{\overline{u'^2 + v'^2}}{2} dp. \quad (1)$$

Here, the overbar denotes the monthly mean and the primes denote deviations therefrom. Note that daily-mean u and v are used and vertical integration is performed along selected 8 pressure levels available in the DAMIP simulations (1000, 850, 700, 500, 250, 100, 50, and 10 hPa). We use daily-mean surface pressure (p_s), but this is replaced with monthly mean when unavailable.

The second metric for storm track intensity is the extratropical cyclone activity (hereafter ECA, Chang et al., 2016; Gertler et al., 2020) representing 24-hr SLP variance defined as follows:

$$ECA = \overline{(\text{SLP}(t + 24\text{hrs}) - \text{SLP}(t))^2}, \quad (2)$$

where SLP(t) is daily-mean SLP. Compared to EKE, ECA represents storm track intensity near the surface.

In addition to storm track metrics, we quantify trends in summertime jet stream using zonal wind at 500 hPa pressure level (hereafter U500 e.g., Coumou et al., 2015). Our results for U500 trends are broadly consistent with Dong et al. (2022), who documented zonal wind trends at 200 hPa.

2.4. Energetic Framework for Regional Storm Tracks

In order to understand the connection between aerosol forcing, which induces trends in surface shortwave radiation over land, and the storm tracks, we use the moist static energy (MSE) framework. The MSE framework can connect surface shortwave radiation and storm track intensity by considering surface energy and atmospheric

(MSE) energy budget equations. The MSE framework has been successfully used to explain the zonal-mean storm track response to changes in shortwave radiation induced by sea ice loss (Shaw & Smith, 2022), the seasonal cycle (Barpanda & Shaw, 2020), as well as the impact of topography and the ocean circulation (Shaw et al., 2022). Here we extend the MSE framework to quantify regional (zonally varying) storm track response to aerosol forcing.

Previous work showed that aerosol emissions and associated aerosol optical depth trends impact surface shortwave radiation over land (Diao et al., 2021; Dong et al., 2022). For example, the decreasing sulfate aerosol emissions and increasing surface shortwave radiation trends over Eurasia and North America can impact the atmospheric energy budget by increasing the surface turbulent (sensible and latent) fluxes, which are connected via the surface energy budget (e.g., Kang et al., 2023; Shaw & Smith, 2022):

$$SW_s = TF + LW_s + NA, \tag{3}$$

where SW_s is the surface shortwave radiation, TF is surface turbulent fluxes, LW_s is the surface longwave radiation, and NA is the non-atmospheric fluxes (e.g., surface heat storage and ocean heat flux divergence). Over land where aerosols impact shortwave radiation, the NA term is negligible since land does not store energy. If LW_s trends are small, increasing surface shortwave radiation (SW_s) trends will be mostly balanced by increasing surface turbulent flux trends (TF) over land.

The aerosol-induced surface turbulent flux trends over land can then impact the atmospheric energy export from land. This relationship can be quantified using the atmospheric MSE (denoted m) budget (Kang et al., 2008; Shaw & Smith, 2022):

$$TF + Ra = \nabla \cdot \mathbf{F} + \partial_t\{h\}, \tag{4}$$

where Ra is the radiative cooling, $\mathbf{F} = \left(\overline{\{um\}}, \overline{\{vm\}}\right)$ is the vertically integrated (denoted $\{\cdot\}$) atmospheric MSE flux divergence, and $\partial_t\{h\}$ is the atmospheric heat storage (h is the moist enthalpy). Note that all terms are in units of W m^{-2}.

Thus, increasing surface turbulent flux trends will lead to increasing atmospheric MSE flux divergence ($\nabla \cdot \mathbf{F}$), suggesting more energy is exported from land, assuming other terms (Ra and $\partial_t\{h\}$) are negligible. The increased contrast in the atmospheric MSE budget between land and ocean strengthens land-to-ocean energy transport. For example, during the spring-to-summer seasonal transition when surface turbulent fluxes over land increase (in response to increased shortwave radiation), energy diverges over land and converges over ocean (Donohoe & Battisti, 2013) showing land-to-ocean energy transport. These ideas describe land-ocean energy coupling in the NH midlatitudes (e.g., Shaw & Voigt, 2015).

The atmospheric MSE flux divergence is accomplished by transient eddies (storm tracks) and stationary circulations,

$$\nabla \cdot \mathbf{F} = \nabla \cdot \mathbf{F_{TE}} + \nabla \cdot \mathbf{F_{SC}}, \tag{5}$$

where $\mathbf{F_{TE}} = \left(\overline{\{u'm'\}}, \overline{\{v'm'\}}\right)$ and $\mathbf{F_{SC}} = (\{\bar{u}\bar{m}\}, \{\bar{v}\bar{m}\})$ are vertically integrated atmospheric MSE flux vectors due to transient eddies (storm tracks) and stationary circulations, respectively. The primes denote deviation from the monthly mean, and $\mathbf{F_{TE}}$ is calculated by multiplying wind and MSE anomalies and integrating the product over 8 pressure levels. Then, $\nabla \cdot \mathbf{F_{SC}}$ is calculated as $\nabla \cdot \mathbf{F} - \nabla \cdot \mathbf{F_{TE}}$ after calculating $\nabla \cdot \mathbf{F}$ from Equation 4. The magnitude of $\mathbf{F_{TE}}$, particularly the meridional component $\overline{\{v'm'\}}$, represents the storm track intensity. Here the stationary circulations include stationary waves, jet stream, and mean meridional circulations. Land-ocean energy coupling is mainly in the zonal direction (Donohoe & Battisti, 2013) and accomplished by the stationary circulation, $\mathbf{F_{SC}}$. The decomposition in Equation 5 also demonstrates the importance of stationary circulations in understanding storm tracks (Barpanda & Shaw, 2017; Kaspi & Schneider, 2013; Shaw et al., 2018).

To connect to the storm tracks, we can isolate the transient eddy component,

$$\nabla \cdot \mathbf{F_{TE}} = TF + Ra - \nabla \cdot \mathbf{F_{SC}} - \partial_t\{h\}, \tag{6}$$

where the regional MSE flux divergence due to storm tracks is connected to surface turbulent fluxes and stationary circulations. The storm track ($\mathbf{F_{TE}}$) response to the change in TF over land and energy transport from $\mathbf{F}_{SC}$ can be determined following (Boos & Korty, 2016),

$$\mathbf{F_{TE}^*} = \nabla\mathcal{L}(TF + Ra - \nabla \cdot \mathbf{F_{SC}} - \partial_t\{h\}), \tag{7}$$

where $\mathcal{L} = \nabla^{-2}$ is the inverse Laplacian operator. The term $\mathbf{F_{TE}}^*$ is an approximate solution to $\mathbf{F_{TE}}$ (~90% of $\mathbf{F_{TE}}$ in regional storm tracks, Figure A1). Further mathematical details explaining the relationship between $\mathbf{F_{TE}}^*$ and $\mathbf{F_{TE}}$ are included in Appendix A. Considering the inverse Laplacian ($\mathcal{L}$) as a negative sign, Equation 7 satisfies the intuition that $\mathbf{F_{TE}}$ points downgradient of the energy flux.

The regional storm track intensity is then defined as $I_{TE} = 2\pi a\cos\phi F_{TE}^{y_s*}$, where a is the Earth's radius and $F_{TE}^{y_s*}$ is the meridional component of $\mathbf{F_{TE}^*}$. The regional storm track intensity, I_{TE}, is similar to $2\pi a\cos\phi\overline{\{v'm'\}}$ (Figure A1). By multiplying $2\pi a\cos\phi$ to Equation 7 and focusing on the meridional component, an equation for regional storm track intensity is obtained.

$$\begin{aligned} I_{TE} &= 2\pi a\cos\phi\partial_y\mathcal{L}(TF + Ra - \nabla \cdot \mathbf{F_{SC}} - \partial_t\{h\}) \\ &= I_{TF} + I_{Ra} - I_{SC} - I_{\partial_t\{h\}} \end{aligned} \tag{8}$$

From above, $-I_{SC} = 2\pi a\cos\phi\partial_y\mathcal{L}(-\nabla \cdot \mathbf{F_{SC}})$ shows that storm track intensity will depend on the meridional gradient of $\mathcal{L}(-\nabla \cdot \mathbf{F_{SC}})$ or similarly $\nabla \cdot \mathbf{F_{SC}}$. Thus, oceanic storm tracks can weaken when stationary circulations converge energy at high latitudes as a result of energy transport from upstream land. All terms have a unit of PW and are defined at every longitude and latitude.

3. Results

3.1. Impact of Anthropogenic Forcings on Summertime Circulation Weakening

3.1.1. Zonal-Mean Trends

The satellite-era summertime circulations quantified by EKE, ECA, and U500 weaken across reanalysis data sets (black, Figures 1a–1c), consistent with trends reported in previous work (Chang et al., 2016; Chemke & Coumou, 2024; Coumou et al., 2015; Dong et al., 2022; Gertler & O'Gorman, 2019; Kang et al., 2023). The weakening trends in reanalysis data sets are statistically significant across most metrics (Figures 1d–1f). The average EKE, ECA, and U500 trends in four reanalyses correspond to weakening of -1.3% decade^{-1}, -1.9% decade^{-1}, and -0.8% decade^{-1}, respectively.

Similar to the reanalyses, EKE, ECA, and U500 all weaken in the DAMIP ALL simulations (purple, Figures 1a–1c) demonstrating model skill in simulating the circulation weakening. For all metrics, the ensemble-mean trends in ALL simulations are close to the average of reanalysis trends (black and purple, Figures 1d–1f). Furthermore, if we give each reanalysis trend a percentile rank in the model ensemble distribution, the average reanalysis ranks in the ALL simulation ensemble are 40.7%, 37.2%, and 50.0% for EKE, ECA, and U500, respectively. This indicates that reanalysis trends sit squarely within the trend distribution of ALL simulation ensemble and thus the ALL simulation ensemble captures the circulation trends in reanalyses.

As the ALL simulations capture the reanalysis circulation trends, we now quantify how much of the weakening is attributable to individual forcings. The ensemble-mean EKE trends in GHG (red, Figure 1d) and AER (blue, Figure 1d) simulations are statistically significant and represent 44.6% and 37.8% of the total weakening trend, respectively. The results do not change if we first average across different realizations in different models and then take the multi-model mean (Figure S1 in Supporting Information S1). The results also do not change if we quantify trends from 1980 to 2006 to account for East Asian aerosol forcing uncertainty (not shown, Zhang et al., 2019; Wang et al., 2021). Similarly, for ECA, the ensemble-mean trends in GHG (red, Figure 1e) and AER (blue, Figure 1e) simulations are statistically significant and respectively represent 45.5% and 46.5% of the total

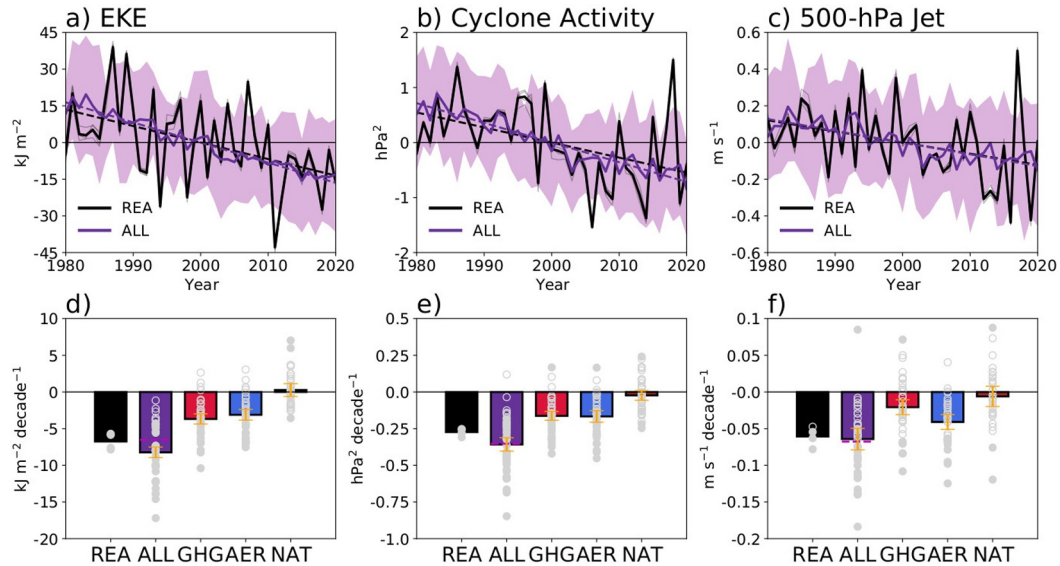

Figure 1. (a–c) Timeseries of Northern Hemisphere (NH) JJA (a) EKE (30–60°N), (b) ECA (30–70°N), and (c) U500 (35–70°N) for reanalysis (black) and ALL simulation ensemble mean (purple) with respect to 1980–2020 climatology. The corresponding linear regressions are shown in dashed lines. The timeseries in individual reanalysis are shown in thin black lines and the 10%–90% model ensemble spread is shaded (d–f) Linear trends of NH JJA (d) EKE, (e) ECA, and (f) U500 from 1980 to 2020 in reanalysis data and Detection and Attribution Model Intercomparison Project simulations. The reanalysis and ensemble mean trends are shown in bars and individual reanalysis and simulation trends are shown in gray circles. The circles are filled if the trends are statistically significant at the 95% confidence level. The 95% confidence intervals for the ensemble mean trend are shown with yellow errorbars. The magenta line indicates the sum of ensemble-mean trends in the single forcing simulations.

weakening trend. For U500, the ensemble-mean trends in GHG (red, Figure 1f) and AER (blue, Figure 1f) simulations are also statistically significant, and respectively represent 32.3% and 63.6% of the total weakening trend. For all metrics, the ensemble-mean trends in NAT simulations are small and statistically insignificant (brown, Figures 1d–1f). The sum of ensemble-mean trends in the single forcing simulations is close to the ALL simulation ensemble-mean trend, indicating the linearity of circulation responses to individual forcings (magenta line and purple bar Figures 1d–1f).

3.1.2. Regional Trends

The storm track weakening, throughout the troposphere (EKE) and at the surface (ECA), exhibits a regional structure with a clear weakening over storm tracks in the Pacific and Atlantic sectors in reanalysis data (Figures 2a and 3a). The ALL simulations also exhibit a weakening of Pacific and Atlantic storm tracks in the ensemble mean (Figures 2b and 3b). The U500 also weakens over Eurasia and the Pacific consistent with Dong et al. (2022), and it weakens with an equatorward shift over the Atlantic (Figure S2 in Supporting Information S1).

Some differences in the spatial structure between the reanalyses and ensemble mean trends are expected because the ensemble mean is an average across different realizations and the reanalysis mean represents a single realization. The positive ECA trends in reanalysis over the Atlantic (Figure 3a) are consistent with Atlantic U500 trends that could steer surface cyclones more toward Europe, which is not well represented in the ALL simulations (Figure S2 in Supporting Information S1, see also Dong & Sutton, 2021).

When considering the Pacific and Atlantic storm track weakening separately, the ensemble-mean trends are close to the reanalysis trends (black and purple, Figures 2e, 2f, 3e, and 3f). The average reanalysis ranks for EKE trends are 30.7% and 57.1% in the ALL simulation ensemble for the Pacific and Atlantic, respectively. The corresponding average reanalysis ranks are also similar for ECA trends (30.1% and 68.5%), indicating that the ALL simulations capture the regional reanalysis storm track trends.

The impacts of greenhouse gas and aerosol forcing on the storm tracks vary regionally (Figures 2c, 2d, 3c, and 3d). In response to greenhouse gas forcing, the Pacific and Atlantic storm tracks weaken similarly for both EKE

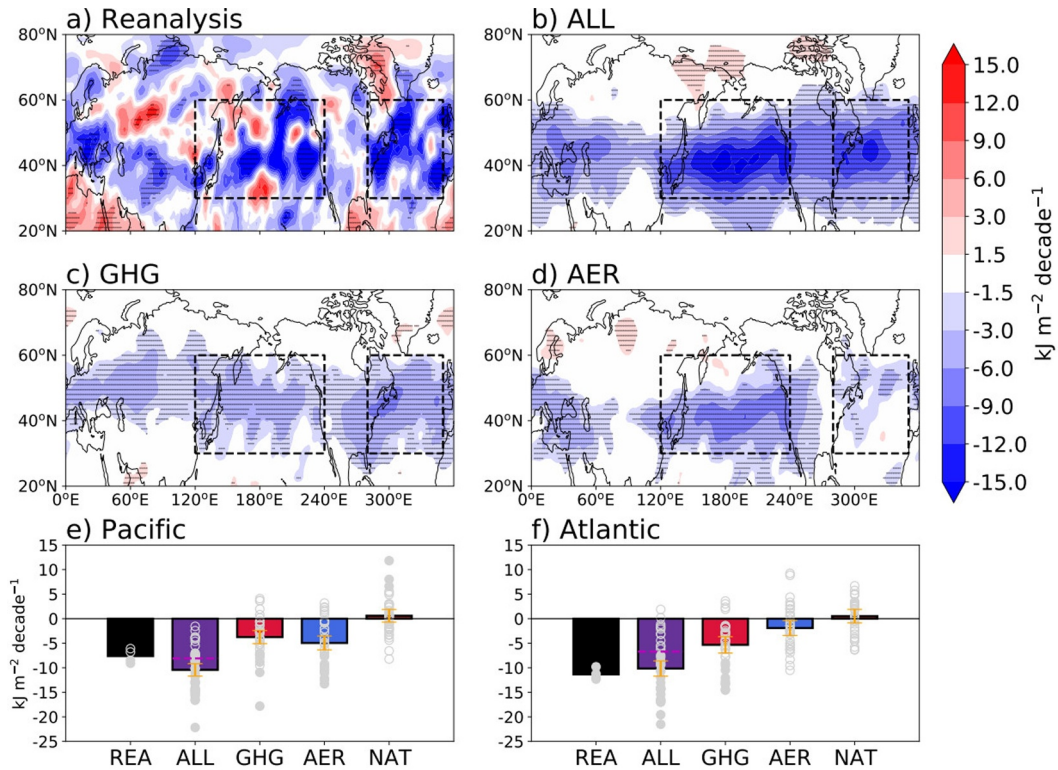

Figure 2. (a–d) Spatial structure of JJA EKE trends from 1980 to 2020 in panel (a) reanalyses mean (CFSR, ERA5, JRA55, and MERRA2) and ensemble-mean (b) ALL, (c) GHG, and (d) AER simulations. Statistically significant trends at the 95% confidence level are stippled. Black dashed lines represent Pacific (30–60°N, 120–240°E) and Atlantic (30–60°N, 280–350°E) storm track domains, respectively (e, f) Similar results to Figure 1d, but for EKE trends averaged in the (e) Pacific and (f) Atlantic storm tracks.

and ECA (Figures 2c, 2e, 2f, 3c, 3e, and 3f). By contrast, in response to aerosol forcing, the storm track weakening in the Pacific is greater than the Atlantic (statistically significant at the 95% level) by 2.6 times for EKE and 1.8 times for ECA (Figures 2d–2f, and 3d–3f).

Consistently, aerosol forcing dominates the weakening of the Pacific storm track, contributing to 47.4% of the total EKE weakening and 57.1% of the total ECA weakening (blue, Figures 2e and 3e). Greenhouse gas forcing, which contributes to 35.9% for EKE and 26.7% for ECA weakening, is secondary (red, Figures 2e and 3e). Greenhouse gas forcing dominates the weakening of the Atlantic storm track, contributing to 52.5% of the total EKE weakening and 50.1% of the total ECA weakening (red, Figures 2f and 3f). The contribution of aerosols to the Atlantic storm track weakening is only 18.9% for EKE and 40.8% for ECA trends (red, Figures 2f and 3f). The ensemble-mean EKE and ECA trends in the NAT simulations are still small and insignificant for both the Pacific and Atlantic sectors. Note that circulation responses to forcings are less linear regionally (magenta dashed lines, Figures 2e, 2f, 3e, and 3f). In general, weakening regional circulation trends are consistent with regional weakening of temperature gradient (Figure S3 in Supporting Information S1).

3.2. Understanding the Aerosol-Induced Storm Track Weakening in the Satellite Era

The results above show that greenhouse gas and aerosol forcings have significantly weakened the regional storm tracks in the satellite era. The storm track weakening from greenhouse gas forcing, which is close to being zonally symmetric, has been discussed in Shaw et al. (2018). Here we investigate how anthropogenic aerosol forcing in the satellite era has weakened the NH summertime storm tracks, especially over the Pacific. We use the regional energetic framework to understand the energetic response to aerosol forcing. We analyze the ensemble-mean trends in the AER simulations in order to focus on the storm track response to aerosol forcing. The trends in reanalysis (ERA5) are broadly consistent with the AER simulations, as we show below, hinting that aerosol-related circulation weakening is operating in the observed trends (e.g., Dong et al., 2022). We mainly use

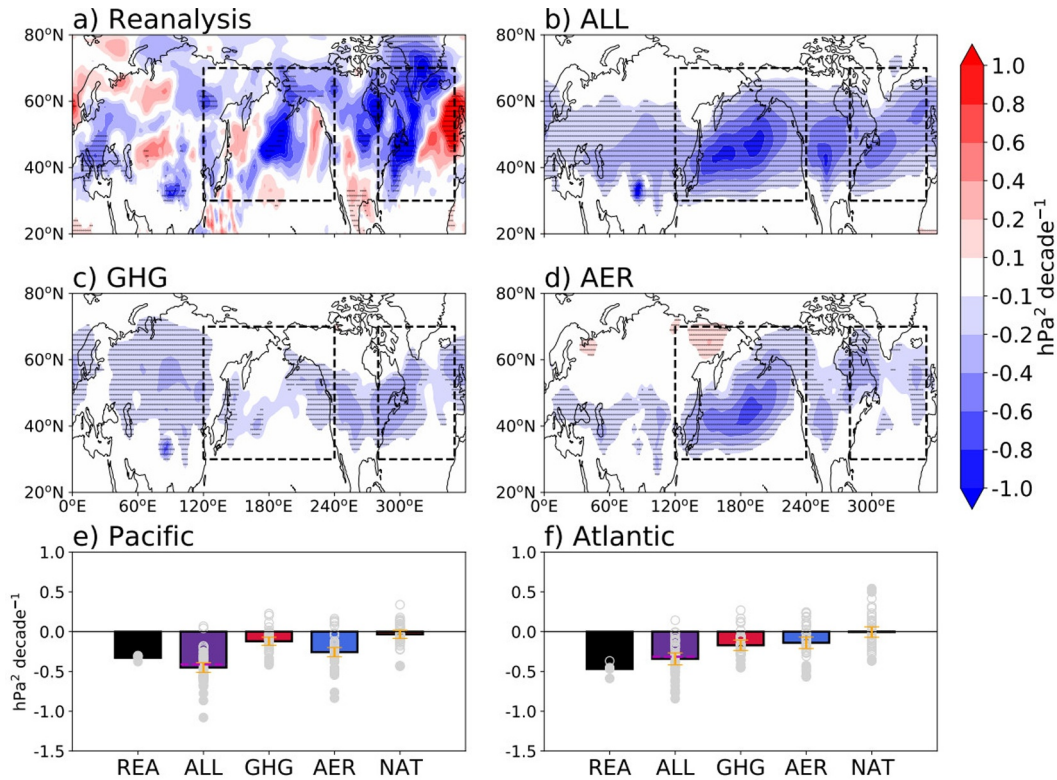

Figure 3. Similar results to Figure 2, but for ECA trends. Black dashed lines represent Pacific (30–70°N, 120–240°E) and Atlantic (30–70°N, 280–350°E) storm track domains, respectively.

ERA5 because they are known for reliable land-to-ocean energy transport climatology (Mayer et al., 2021) and surface turbulent flux over NH midlatitude land (Martens et al., 2020). We investigate how (a) aerosol emission trends over land impact the storm tracks downstream and (b) why the storm track weakening is greater over the Pacific sector than the Atlantic sector (Figures 2d and 3d).

3.2.1. Aerosol-Induced Surface Energy Budget Trends

In response to aerosol forcing, clear-sky surface shortwave radiation shows a positive trend over the Eurasian continent from Europe to central Asia (hereafter Eurasia) and North America and shows a negative trend over South and East Asia (Figure 4a). This pattern is consistent with aerosol emissions and aerosol optical depth trends in these regions (Klimont et al., 2013; Quaas et al., 2022). By contrast, greenhouse gas forcing drives a positive shortwave radiation trend over the Arctic and Tibetan Plateau but has minimal impact over most of NH land (Figure 4b). The aerosol forcing dominates the clear-sky surface shortwave radiation trends over NH land in the ALL simulation ensemble (Figure 4c, see also Dong et al., 2022; Hodnebrog et al., 2024), which reasonably reproduces the trends in reanalysis (Figure 4d). Similar patterns of trends are also found at the top of the atmosphere (Figure S4 in Supporting Information S1). The reanalysis (ERA5) shortwave radiation trends agree reasonably with CERES trends (Figure S5 in Supporting Information S1) over a shorter period.

The all-sky surface shortwave radiation trends due to aerosol forcing (Figure 5a) strongly resemble the clear-sky radiation trends (Figure 4a). In particular, the spatial pattern correlation coefficient between the clear-sky and all-sky surface shortwave radiation trends is 0.93 over 10°–70°N. The clear-sky radiation contributes to about 65% of increasing surface shortwave radiation trends over Eurasia and North America and contributes to about 100% of decreasing surface shortwave radiation trends over South and East Asia. This indicates that the direct aerosol effect dominates the response to aerosol forcing, particularly over land. In contrast, over the North Pacific (20°–30°N), aerosol-cloud interaction is important as noted in previous work (Wang et al., 2014).

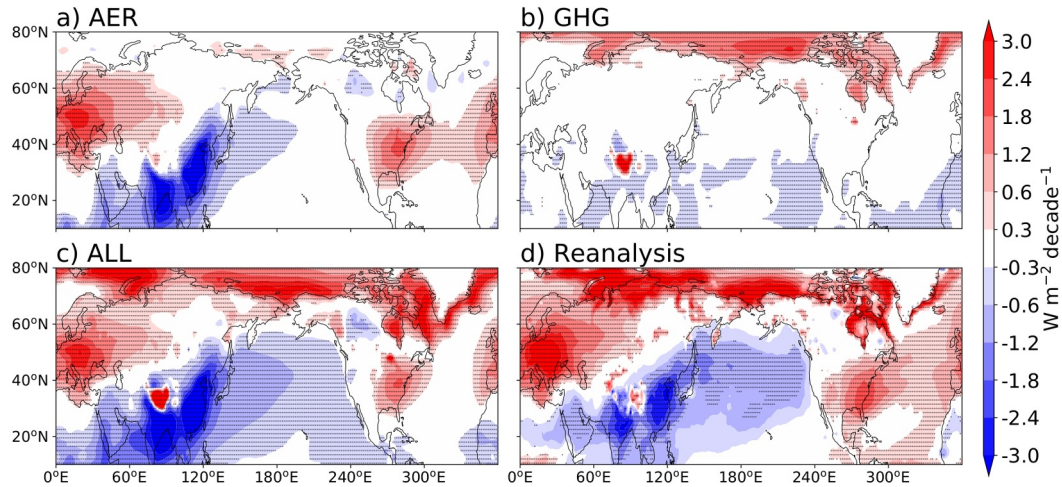

Figure 4. Spatial structure of JJA cosine-weighted trend from 1980 to 2020 of clear-sky surface shortwave radiation in ensemble-mean (a) AER, (b) GHG and (c) ALL simulations, and in panel (d) reanalysis (ERA5). Statistically significant trends at the 95% confidence level are stippled.

The aerosol-induced trends in (all-sky) surface shortwave radiation over Eurasia, North America, and South and East Asia are balanced by surface turbulent flux trends (Figure 5b) according to the surface energy budget with roughly equal contributions from latent and sensible heat flux. The spatial pattern correlation coefficient between surface shortwave radiation and turbulent flux trends is 0.87 over 10°–70°N. In other words, $\Delta TF \approx \Delta SW_s \approx \Delta SW_{s,clearsky}$ from Equation 3, where Δ denotes the linear trend. Interestingly, a similar surface energy balance was seen in response to Arctic sea ice loss except in that case the balance is over the ocean (Shaw & Smith, 2022). The surface turbulent flux trends spatially integrated over the area with positive trends are 2.4 times larger in Eurasia (40°–70°N) than in North America (30°–60°N), due to larger area of decreased emissions in Eurasia (Figures 6a and 6b). Consistently, positive surface turbulent flux trends which are greater over Eurasia are also found in reanalysis trends (Figure S6 in Supporting Information S1).

3.2.2. Aerosol-Induced MSE Budget and Storm Track Trends

The positive surface turbulent flux trend over Eurasia and North America due to changes in the surface shortwave radiation increases the land-to-ocean atmospheric energy contrast. Since the impacts of radiative cooling (Ra) and atmospheric heat storage ($\partial_t\{h\}$) are negligible (Figures 5c, 6a, 6b, and 6d–6e), the increased land-to-ocean atmospheric energy contrast strengthens land-to-ocean energy transport indicated by positive and negative $\nabla \cdot \mathbf{F}$ trends over land and ocean, respectively (Figure 5d). The land-to-ocean energy transport trends are dominated primarily by the stationary circulation (Figure 5e and red in Figures 6a and 6b), resulting in noticeable MSE flux convergence trends poleward of the Pacific and Atlantic storm tracks. The land-to-ocean energy transport trends are about 1.6 times larger in Eurasia-Pacific than North America-Atlantic, as indicated by the differences in area-integrated $\nabla \cdot \mathbf{F}_{\mathbf{SC}}$ trends over land (Figures 6a and 6b) and downstream ocean (Figures 6d and 6e). Similar to the response to aerosol forcing, energy export trends over land due to stationary circulations are found in reanalysis (Figure S6 in Supporting Information S1).

Over South and East Asia, the negative surface turbulent flux trends are largely compensated by a negative radiative cooling trend (Figure 5c), that is consistent with increasing shortwave-absorbing aerosol (e.g., black carbon) emissions in the region (Hoesly et al., 2018). Nevertheless, the remaining negative energy trend decreases the land-to-ocean energy contrast and weakens the land-to-ocean energy transport by stationary circulations, indicated by negative and positive $\nabla \cdot \mathbf{F}_{\mathbf{SC}}$ (also $\nabla \cdot \mathbf{F}$) trends over land and ocean, respectively (Figures 5d and 5e). This results in an MSE flux divergence trend equatorward of the Pacific storm track (Figure 5e). Consequently, the MSE flux divergence/convergence trends due to stationary circulations over the Pacific (Figure 5e) exhibit a pronounced meridional dipole. The dipole trend is compensated by MSE flux divergence/convergence trends due to transient eddies (Figure 5f).

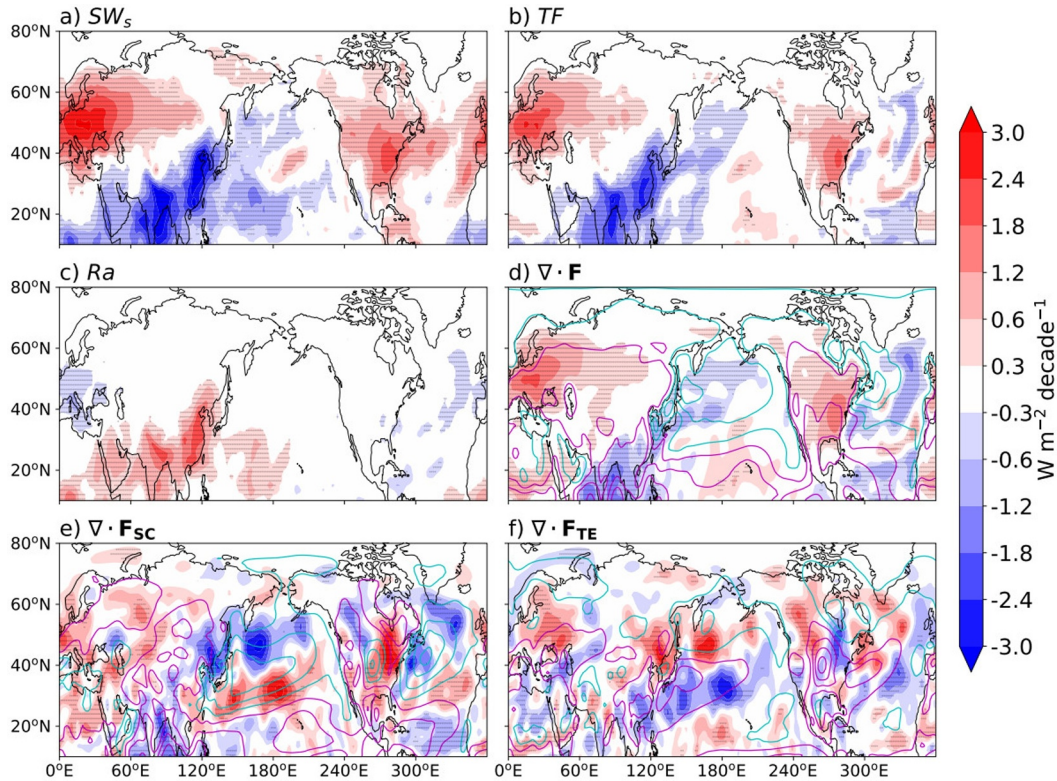

Figure 5. Spatial structure of JJA cosine-weighted ensemble-mean trends from 1980 to 2020 of (a) all-sky surface shortwave radiation, (b) surface turbulent flux, (c) radiative cooling, (d) moist static energy (MSE) flux divergence, (e) MSE flux divergence due to stationary circulations, and (f) MSE flux divergence due to transient eddies in the AER simulations with global mean removed. Statistically significant trends at the 95% confidence level are stippled. In panels (d–f), summertime climatology is shown in magenta and cyan contours for MSE flux divergence and convergence, respectively (from 15 W m^{-2} in 30 W m^{-2} intervals), and the trends are smoothed at T63 using a filter from Sardeshmukh and Hoskins (1984).

As strengthened land-to-ocean energy transports by stationary circulations converge energy poleward of the storm tracks, the poleward energy transport from the storm tracks can weaken. Furthermore, over the Pacific, the weakened land-to-ocean energy transport between South and East Asia and the Pacific, diverges energy equatorward of the storm track, further demanding the poleward energy transport from the storm tracks to weaken. This connection between energy transport from the storm tracks (i.e., storm track intensity) and changes in regional meridional energy gradient are quantified using Equation 8.

The regional storm track intensity, defined as I_{TE}, weakens significantly due to aerosol forcing (Figure 7a), and the weakening over the Pacific is greater than that in the Atlantic by 2.0 times (black, Figure 7d), similar to EKE and ECA trends (Figures 2d and 3d). Consistent with the regional energy gradient trend contributed by stationary circulations (Figure 6e), both Pacific and Atlantic storm tracks weaken due to stationary circulations (Figure 7b). Quantitatively, the stationary circulations contribute to 60.6% and 48.3% of the weakening over the Pacific and Atlantic, respectively (red, Figure 7d). The surface turbulent flux also significantly contributes to the storm track weakening near the coastlines of upstream land (Figure 7c). They contribute to 49.4% and 34.4% of the weakening over the Pacific and Atlantic, respectively (blue, Figure 7d). Note also over southern and eastern Europe, the storm track weakening is dominated by surface turbulent flux contribution (Figures 7a and 7c). While the contribution from the surface turbulent fluxes is maximized over land in East Asia (Figure 7c), the storm track weakening there is not as strong since there is a strong cancellation from stationary circulation contribution (Figure 7b). The contributions from radiative cooling and atmospheric storage are small for both storm tracks (pink and gray, Figure 7d).

The difference between the Pacific and Atlantic storm track trends is also contributed by both stationary circulations and surface turbulent fluxes (Figure 7d). Two factors can be responsible for the difference. First is the

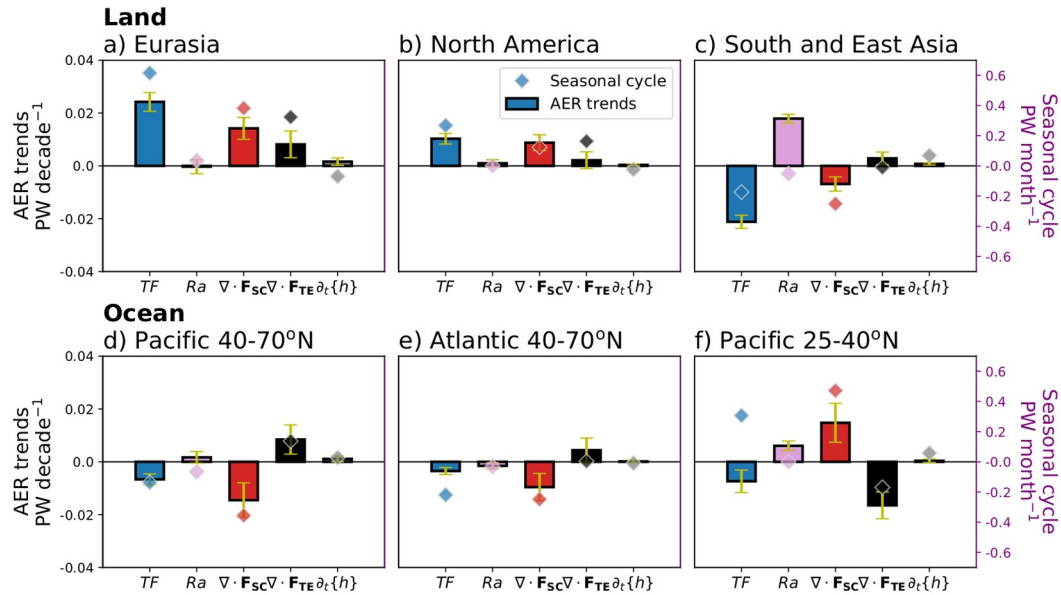

Figure 6. (Bars, left axis) Ensemble-mean JJA trends (1980–2020) in the AER simulations and (diamonds, right axis) seasonal transition in ERA5 of the moist static energy budget integrated across (a–c) upstream land and (d–f) downstream ocean: (a) Eurasia land (40–70°N) where $\Delta TF > 0$, (b) North America land (30–60°N) where $\Delta TF > 0$, (c) South and East Asia land (10–40°N, 60–140°E) where $\Delta TF < 0$, (d) Pacific 40–70°N, (e) Atlantic 40–70°N, and (f) Pacific 25–40°N. The 95% confidence intervals for the ensemble-mean trend are shown with yellow errorbars. In panels (a, b, d,and e), the seasonal transition is shown for June minus May and in panels (c, f) it is shown for December minus November.

difference in the positive surface shortwave radiation trends due to aerosol forcing over the land upstream, which are greater over Eurasian than North America. Second is the negative surface shortwave radiation trends due to aerosol forcing in the South and East Asia. To demonstrate the importance of the second factor, we investigate the aerosol-induced trends during 41 years prior to the satellite era (1940–1980), when aerosol (shortwave-reflecting) emissions have been increasing in all NH land (Hoesly et al., 2018; Undorf et al., 2018). During this period when there is no surface shortwave trend dipole across Eurasia and South and East Asia, the storm track trends between the Pacific and Atlantic are comparable (Figure S7 in Supporting Information S1).

Similar connections between changes in shortwave forcing, surface turbulent fluxes, land-to-ocean energy transport, and the storm tracks are seen in the seasonal cycle (Figure 6). During the seasonal transition from spring to summer when surface shortwave radiation increases over Eurasia and North America, the increased surface turbulent flux from land strengthens the land-to-ocean energy contrast (blue diamonds, Figures 6a, 6b, and 6d–6e, see Figure S8 in Supporting Information S1 for spatial pattern). Then, land-to-ocean energy transport from stationary circulations also increases (e.g., Donohoe & Battisti, 2013), converging energy poleward of the oceanic storm tracks (red diamonds, Figures 6a, 6b, and 6d–6e). Consequently, the storm tracks compensate for the energy flux convergence from stationary circulations (black diamonds, Figures 6a, 6b, and 6d–6e), which corresponds to storm track weakening. The opposite is true for South and East Asia during the seasonal transition from fall to winter when land-to-ocean energy contrast and transport from stationary circulations weaken (diamonds, Figures 6c and 6f, see Figure S9 in Supporting Information S1 for spatial pattern). Thus, the aerosol-induced stationary circulation trends, which advects energy from land to ocean, can be understood in line with the response to increasing land-to-ocean energy contrast (Shaw & Voigt, 2015).

3.2.3. Prediction of Aerosol-Induced Storm Track Trends

By analyzing the energy budget changes in AER simulations and observed seasonal cycle, we identified three key processes that are responsible for aerosol-induced storm track weakening. Here we build a theoretical model using Equation 6 and the three key processes to predict the storm track response to aerosol forcing.

First, the aerosol-induced positive shortwave radiation trends over land induce surface turbulent flux trends that strengthen land-to-ocean energy transport from stationary circulation. This can be written as

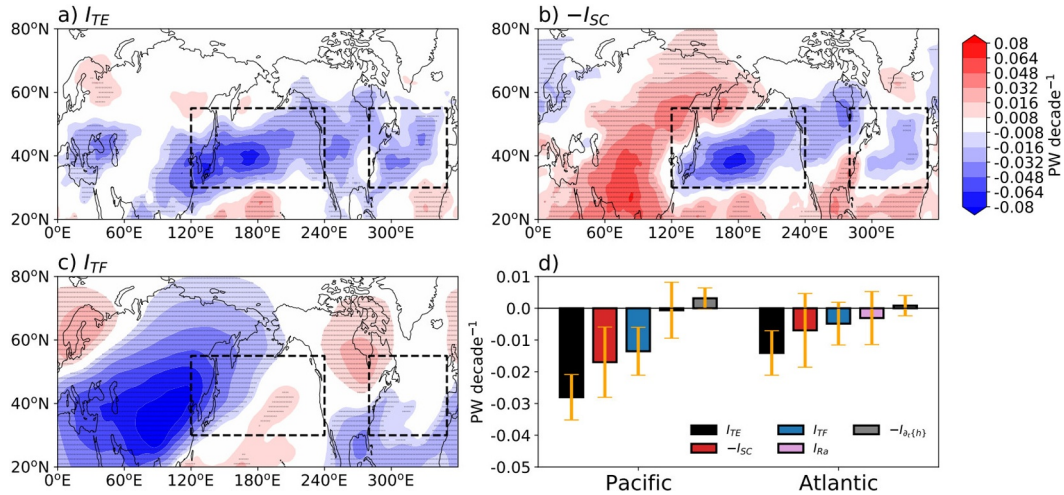

Figure 7. Spatial structure of JJA ensemble-mean trends from 1980 to 2020 of (a) storm track intensity (I_{TE}) and contributions from (b) stationary circulation ($-I_{SC}$) and (c) surface turbulent fluxes (I_{TF}) from the AER simulations. Statistically significant trends at the 95% confidence interval are stippled. The Pacific (30–55°N, 120–240°E) and Atlantic (30–55°N, 280–350°E) storm track domains are shown in black dashed box. (d) The ensemble-mean JJA storm track trends from 1980 to 2020 and their decomposition in the Pacific and Atlantic from the AER simulations. The 95% confidence intervals are shown with yellow errorbars.

$$\Delta TF_L = \Delta(\nabla \cdot \mathbf{F_{SC}})_L, \tag{9}$$

where subscript L is for land and Δ denotes the linear trend. Second, strengthened land-to-ocean energy transport from stationary circulation converges energy poleward of the oceanic storm tracks. To represent this, we define

$$-\frac{A_L}{A_O}\Delta\langle \nabla \cdot \mathbf{F_{SC}}\rangle_L = \Delta(\nabla \cdot \mathbf{F_{SC}})_O, \tag{10}$$

where subscript O is for ocean, $\langle \cdot \rangle$ represents an area average and A_L and A_O denote the area of upstream land and downstream ocean, respectively. This simplification means that energy diverged over upstream land all converges in the downstream ocean. The MSE flux convergence due to stationary circulations is set identically at every grid point in each ocean sector (Figure 8b). Although the simulated trends are different from being constant over the ocean sector (Figure 5e), this design is to represent the impact of land-ocean energy coupling at the most simplified level. Third, storm tracks compensate for the energy convergence due to stationary circulations over the ocean. This is simply modeled as (Figure 8c):

$$\Delta(\nabla \cdot \mathbf{F_{SC}})_O = -\Delta(\nabla \cdot \mathbf{F_{TE}})_O. \tag{11}$$

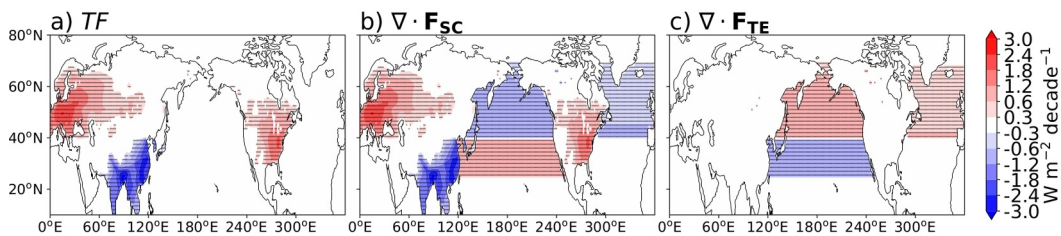

Figure 8. Spatial structure of JJA cosine-weighted trends from 1980 to 2020 in the theoretical model for (a) surface turbulent flux, (b) moist static energy (MSE) flux divergence due to stationary circulations, and (c) MSE flux divergence due to transient eddies. The trends in panel (a) are taken from the AER simulations over Eurasia, North America, and South and East Asia. The slight difference between Figure 6a and (a) is because the global-mean trend is removed in Figure 5a. Statistically significant trends at the 95% confidence interval are stippled.

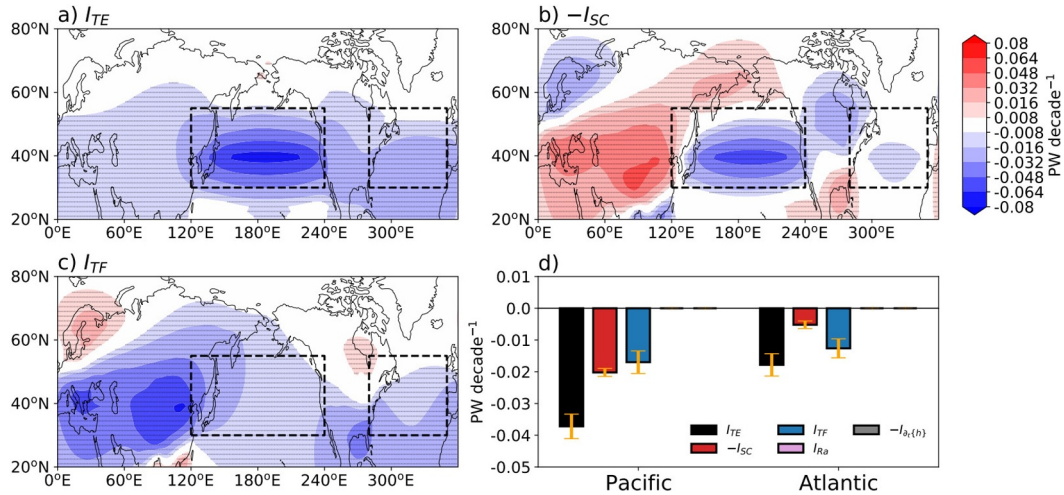

Figure 9. Similar results to Figure 7, but for trends predicted from the theoretical model. In panel (d), the trends due to radiative cooling (I_{Ra}) and atmospheric heat storage ($-I_{\partial_t\{h\}}$) are zero.

To make quantitative prediction of the storm track response using the theoretical model (Equations 9–11), we consider three upstream land sectors (as in Figures 6a–6c), Eurasia (40–70°N), North America (30–60°N), and South and East Asia (10–40°N and 60–140°E). We also consider three corresponding downstream ocean sectors (as in Figures 6d–6f), Pacific 40°–70°N, Atlantic 40°–70°N, and Pacific 25°–40°N. The selected upstream land and downstream ocean sectors take into account the dominant pattern of land-to-ocean MSE flux trends due to aerosol forcing and their climatology (magenta and cyan lines in Figures 5d and 6e).

We take surface turbulent flux trends from the AER simulations (Figure 8a) as an input to this theoretical model (ΔTF_L in Equation 9). When the left-hand side of Equation 9 is known, all terms in Equations 9–11 can be calculated, and the statistical significance of the predicted trend is determined from this term. Lastly, when the regional trends in MSE budgets are built (Equations 9–11), the storm track trend is predicted using Equation 8.

The storm track trends predicted from the theoretical model exhibit weakening over the Pacific and Atlantic sectors (Figure 9a) as in the AER simulations (Figure 7a). Although slightly overestimated, the storm track trends from the theoretical model well resemble the spatial pattern of trends in the AER simulations with a spatial correlation coefficient of 0.61 over 20–70°N. The Pacific storm track weakens about 2.1 times more than the Atlantic storm track according to the prediction (compare black bars in Figure 9d), consistent with the AER simulations (2.0 times, Figure 9d). The slight overestimation can be related to applying Equation 9 over South and East Asia where the radiative cooling trend is also important.

The relative contributions of stationary circulations (Figure 9b) and surface turbulent fluxes (Figure 9c) predicted by the theoretical model are consistent with AER simulations over the Pacific (Figures 7d and 7d). In the Atlantic, the relative contributions are less consistent between theoretical models and AER simulations, but the trends in AER simulations are not statistically significant there (Figures 7d and 9d). Overall, the similarities between the predicted trends and the actual AER simulation confirm that processes represented by Equations 9–11 accurately capture the storm track weakening from aerosol forcing.

Given the skill of the theoretical prediction, we can use it to understand what leads to greater storm track weakening in the Pacific than in the Atlantic in response to aerosol forcing. We first test the impact of aerosol forcing over South and East Asia by reducing the surface turbulent flux trends there by half. The resulting storm track trends still show greater weakening in the Pacific than in the Atlantic (Figure 10a), but only by 1.6 times (as compared to 2.1 times in Figure 9). We then test the impact of greater aerosol forcing over Eurasia than North America by additionally reducing the surface turbulent flux trends over Eurasia by half. When Eurasian aerosol forcing is halved, the storm track trends in the Pacific and Atlantic become more comparable (their ratio is 1.4, Figure 10b). This indicates that larger aerosol-induced positive surface shortwave radiation trends over Eurasia than North America and negative surface shortwave radiation trends over South and East Asia both contribute to greater storm track weakening over the Pacific than the Atlantic.

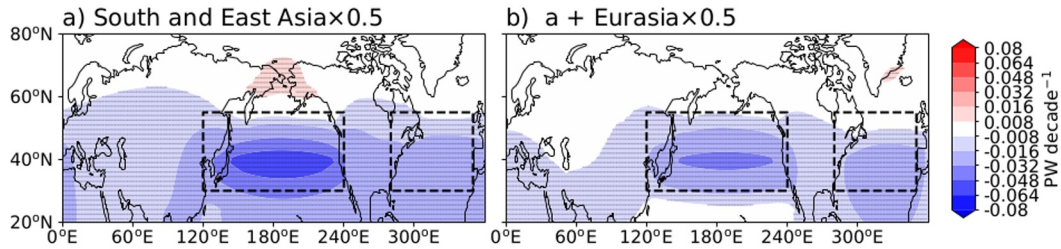

Figure 10. Similar results to Figure 9a, but from theoretical model predictions (a) with aerosol forcing over South and East Asia reduced to half and (b) aerosol forcing over Eurasia also reduced to half. Statistically significant trends at the 95% confidence interval are stippled.

4. Summary and Discussions

The summertime regional circulation in the NH has significantly weakened during the satellite era with important implications for extreme weather. Here we quantify the drivers of the regional circulation weakening and employ an energetic framework to understand the underlying mechanisms. We show that anthropogenic aerosols and greenhouse gas forcings contribute roughly equally to regional circulation weakening in the satellite era according to single-forcing DAMIP simulations. Moreover, the storm track weakening from anthropogenic aerosol forcing is about two times greater in the Pacific than in the Atlantic. This regional impact of aerosol forcing makes it the leading contributor to storm track weakening in the Pacific (about 54%), consistent with its impact on the upper-level Eurasian jet stream (Dong et al., 2022; Undorf et al., 2018).

Using a regional energetic framework (e.g., Boos & Korty, 2016), we show that aerosol-induced shortwave radiation trends over land weaken the storm tracks by driving changes in land-to-ocean energy transport. The increasing surface shortwave radiation trends (dominated by clear-sky radiation) due to decreasing sulfate aerosol emissions over Eurasia and North America are balanced by increasing surface turbulent flux trends into the atmosphere. The positive surface turbulent flux trends strengthen the land-to-ocean energy contrast and the excessive energy over land is transported downstream via stationary circulations. This converges energy poleward of the storm tracks, weakening the poleward energy transport by the storm tracks, thus weakening the storm tracks. This process is about twice as strong in the Eurasia-Pacific sector than in the North America-Atlantic sector because emission trends are larger over Eurasia. Additionally, increasing aerosol emissions over South and East Asia lead to a similar but opposite behavior: decreasing surface shortwave radiation and turbulent flux trends weaken the land-to-ocean energy contrast and transport via stationary circulations. As a result, energy diverges equatorward of the Pacific storm track, demanding the poleward energy transport by the storm track to weaken, and the Pacific storm track further weakens.

We use the underlying energetic balances to create a theoretical model that predicts the storm track weakening trend given the surface turbulent flux trends over land. With this theoretical model, we show that greater negative emission trends over Eurasian than North America and positive aerosol emission trends over South and East Asia lead to larger storm track weakening over the Pacific. The importance of positive aerosol emission trends over South and East Asia for different circulation responses between the Pacific and Atlantic is consistent with previous work for annual mean temperature (Diao et al., 2021; Kang et al., 2021). While previous work noted that aerosol-induced negative shortwave trends over East Asia are overestimated in the CMIP6 models after 2007 (Wang et al., 2021; Zhang et al., 2019), our theoretical modeling approach suggests that the actual response can be predicted by rescaling the overestimated forcing. Our results also suggest that aerosol-radiation interactions are important for summertime Pacific storm track trends, unlike the wintertime when aerosol-cloud interaction is also important (Wang et al., 2014; Zhang et al., 2007).

The significant impact of aerosols on the summertime regional storm tracks is in agreement with previous work showing the impact on regional jet stream (Dong et al., 2022). Previous work also showed Arctic sea ice loss could not explain the recent summertime circulation weakening in the NH (Kang et al., 2023). Consistently there is negligible Arctic sea ice loss in response to aerosol forcing (Figure S10 in Supporting Information S1). In addition, the storm track weakening trends across reanalysis and DAMIP simulations are not correlated with modes of internal variability (e.g., Interdecadal Pacific Oscillation, Figure S11 in Supporting Information S1),

indicating that summertime circulation weakening is likely an anthropogenically forced response (Chemke & Coumou, 2024).

Our regional energetic analysis highlights the importance of stationary circulations in shaping the response of the storm tracks to external forcing in the NH (Barpanda & Shaw, 2017; Kaspi & Schneider, 2013; Shaw et al., 2018). The role of stationary circulation in controlling the storm track response to aerosol forcing is analogous to the seasonal transition from spring to summer, especially over the Pacific (Figure S8 in Supporting Information S1). Both processes involve surface shortwave radiation changes balanced by surface turbulent fluxes, which induce a stationary circulation to export energy downstream on the poleward side of the storm tracks. The similarity of the mechanisms operating seasonally and in response to aerosol forcing suggests the possibility of an emergent constraint, something that will be investigated in future work.

The significant role of anthropogenic aerosols in shaping summertime circulation trends in the satellite era suggests that future summertime circulation will also depend on future emissions of anthropogenic aerosols (Persad et al., 2022). Moreover, since the circulation response to aerosol forcing is primarily through changes in shortwave radiation, the results here provide valuable insights into understanding circulation changes under solar geoengineering scenarios (Gertler et al., 2020) and volcanic eruptions (DallaSanta et al., 2019).

Appendix A: Regional Storm Track Intensity

The regional MSE budget (Equation 6) only describes the divergence of $\mathbf{F_{TE}}$ and a unique solution for $\mathbf{F_{TE}}$ can not be obtained because there are two unknowns (i.e., zonal and meridional components of $\mathbf{F_{TE}}$). To get a unique solution, we replace $\mathbf{F_{TE}}$ with its divergent component $\mathbf{F^*_{TE}}$ in Equation 6. This is a useful approach, since $\mathbf{F_{TE}}$ and $\mathbf{F^*_{TE}}$, and particularly their meridional components, are very close (Figure A1). This means that MSE flux due to storm tracks are mostly divergent.

Then, we introduce an "energy flux potential" (Boos & Korty, 2016), χ, associated with $\mathbf{F^*_{TE}}$ that satisfies

$$\mathbf{F^*_{TE}} = \nabla\chi. \tag{A1}$$

The energy flux potential, χ, has a unit of PW and indicates that energy will flux from low to high χ. Since $\nabla\cdot\mathbf{F^*_{TE}} = \nabla\cdot\mathbf{F_{TE}}$ and $\nabla\cdot\mathbf{F^*_{TE}} = \nabla^2\chi$, the following relationship can be derived,

$$\begin{aligned}\nabla\cdot\mathbf{F_{TE}} &= \nabla^2\chi\\ \chi &= \mathcal{L}(\nabla\cdot\mathbf{F_{TE}}),\end{aligned} \tag{A2}$$

where $\mathcal{L}$ is the inverse Laplacian operator. Thus, combining Equations A1 and A2 results in

$$\mathbf{F_{TE}}^* = \nabla\chi = \nabla\mathcal{L}(\nabla\cdot\mathbf{F_{TE}}). \tag{A3}$$

Combining Equations A3 and 6 results in Equation 7 in Section 2. Lastly, taking the meridional component from Equation A3 and multiplying $2\pi a\cos\phi$ leads to the left-hand side of Equation 8.

$$I_{TE} = 2\pi a\cos\phi\,\partial_y\mathcal{L}(\nabla\cdot\mathbf{F_{TE}}) \tag{A4}$$

The regional storm track intensity, I_{TE}, well represents the climatological storm tracks (Figure A1d). Moreover, the aerosol-induced I_{TE} trends (Figure 7a) resemble EKE and ECA trends (Figures 2d and 3d), with spatial correlation coefficients of 0.68 and 0.59, respectively.

While we note that the concept of "energy flux potential" that focus on the divergent component is very useful in describing energy flux due to storm tracks, the total energy flux $\mathbf{F}$ and the stationary circulation energy flux $\mathbf{F_{SC}}$ are dominated by non-divergent component in midlatitudes.

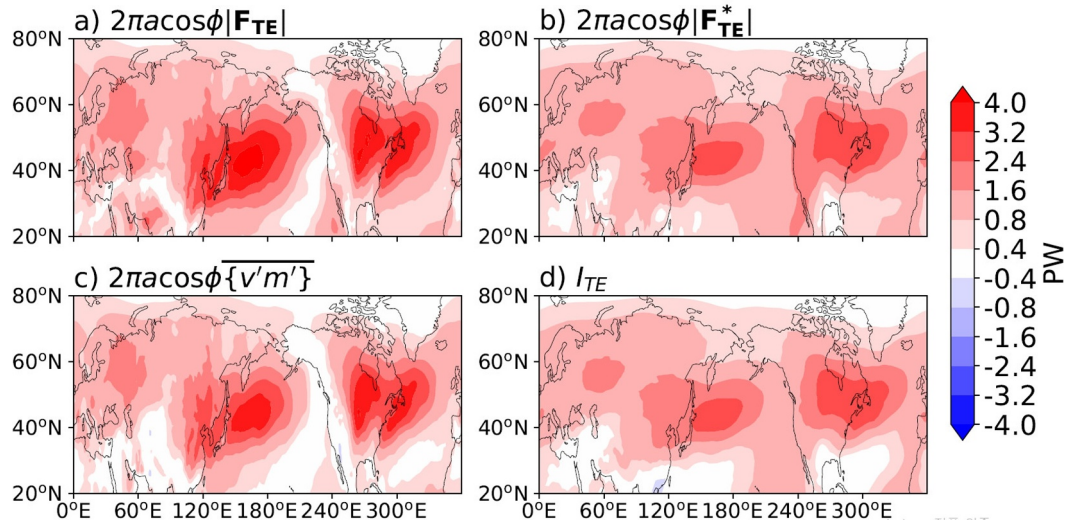

Figure A1. JJA climatology of (a) $2\pi a\cos\phi|\mathbf{F_{TE}}|$, (b) $2\pi a\cos\phi|\mathbf{F_{TE}}^*|$, (c) $2\pi a\cos\phi\overline{\{v'm'\}}$, and (d) I_{TE} from ERA5 (1980–2020). In panels (a, b) absolute values of the flux vectors are shown, and (c, d) show the meridional component. I_{TE} is used as a definition of regional storm tracks.

Conflict of Interest

The authors declare no conflicts of interest relevant to this study.

Data Availability Statement

[Dataset] CFSR reanalysis data are available via Saha et al. (2010, 2011) [Dataset] ERA5 reanalysis data are available via Hersbach et al. (2023) [Dataset] JRA3Q reanalysis data is available via Japan Meteorological Agency (2023) [Dataset] MERRA-2 reanalysis data is available via Global Modeling and Assimilation Office (GMAO) (2015) [Dataset] CMIP6 DAMIP simulations are downloadable from the CMIP6 data search interface https://esgf-node.llnl.gov/search/cmip6/ [Dataset] The data sets supporting the conclusion of this work are available at Kang (2024).

Acknowledgments
JMK, TAS, and LS are supported by NSF-AGS2300037.

References

Allen, R. J., & Sherwood, S. C. (2011). The impact of natural versus anthropogenic aerosols on atmospheric circulation in the community atmosphere model. *Climate Dynamics*, *36*(9–10), 1959–1978. https://doi.org/10.1007/s00382-010-0898-8

Barpanda, P., & Shaw, T. (2017). Using the moist static energy budget to understand storm-track shifts across a range of time scales. *Journal of the Atmospheric Sciences*, *74*(8), 2427–2446. https://doi.org/10.1175/jas-d-17-0022.1

Barpanda, P., & Shaw, T. A. (2020). Surface fluxes modulate the seasonality of zonal-mean storm tracks. *Journal of the Atmospheric Sciences*, *77*(2), 753–779. https://doi.org/10.1175/jas-d-19-0139.1

Boos, W. R., & Korty, R. L. (2016). Regional energy budget control of the intertropical convergence zone and application to mid-Holocene rainfall. *Nature Geoscience*, *9*(12), 892–897. https://doi.org/10.1038/ngeo2833

Chang, E. K., Ma, C.-G., Zheng, C., & Yau, A. M. (2016). Observed and projected decrease in Northern Hemisphere extratropical cyclone activity in summer and its impacts on maximum temperature. *Geophysical Research Letters*, *43*(5), 2200–2208. https://doi.org/10.1002/2016gl068172

Chemke, R., & Coumou, D. (2024). Human influence on the recent weakening of storm tracks in boreal summer. *npj Climate and Atmospheric Science*, *7*(1), 86. https://doi.org/10.1038/s41612-024-00640-2

Coumou, D., Di Capua, G., Vavrus, S., Wang, L., & Wang, S. (2018). The influence of Arctic amplification on mid-latitude summer circulation. *Nature Communications*, *9*(1), 1–12. https://doi.org/10.1038/s41467-018-05256-8

Coumou, D., Lehmann, J., & Beckmann, J. (2015). The weakening summer circulation in the Northern Hemisphere mid-latitudes. *Science*, *348*(6232), 324–327. https://doi.org/10.1126/science.1261768

DallaSanta, K., Gerber, E. P., & Toohey, M. (2019). The circulation response to volcanic eruptions: The key roles of stratospheric warming and eddy interactions. *Journal of Climate*, *32*(4), 1101–1120. https://doi.org/10.1175/jcli-d-18-0099.1

Danabasoglu, G., Lamarque, J.-F., Bacmeister, J., Bailey, D., DuVivier, A., Edwards, J., et al. (2020). The community earth system model version 2 (CESM2). *Journal of Advances in Modeling Earth Systems*, *12*(2), e2019MS001916. https://doi.org/10.1029/2019ms001916

Deser, C., Lehner, F., Rodgers, K. B., Ault, T., Delworth, T. L., DiNezio, P. N., et al. (2020). Insights from Earth system model initial-condition large ensembles and future prospects. *Nature Climate Change*, *10*(4), 277–286. https://doi.org/10.1038/s41558-020-0731-2

Diao, C., Xu, Y., & Xie, S.-P. (2021). Anthropogenic aerosol effects on tropospheric circulation and sea surface temperature (1980–2020): Separating the role of zonally asymmetric forcings. *Atmospheric Chemistry and Physics*, *21*(24), 18499–18518. https://doi.org/10.5194/acp-21-18499-2021

Dong, B., & Sutton, R. T. (2021). Recent trends in summer atmospheric circulation in the North Atlantic/European region: Is there a role for anthropogenic aerosols? *Journal of Climate*, *34*(16), 6777–6795.

Dong, B., Sutton, R. T., Shaffrey, L., & Harvey, B. (2022). Recent decadal weakening of the summer Eurasian westerly jet attributable to anthropogenic aerosol emissions. *Nature Communications*, *13*(1), 1–10. https://doi.org/10.1038/s41467-022-28816-5

Donohoe, A., & Battisti, D. S. (2013). The seasonal cycle of atmospheric heating and temperature. *Journal of Climate*, *26*(14), 4962–4980. https://doi.org/10.1175/jcli-d-12-00713.1

Dow, W. J., Maycock, A. C., Lofverstrom, M., & Smith, C. J. (2021). The effect of anthropogenic aerosols on the Aleutian low. *Journal of Climate*, *34*(5), 1725–1741. https://doi.org/10.1175/jcli-d-20-0423.1

Eyring, V., Bony, S., Meehl, G. A., Senior, C. A., Stevens, B., Stouffer, R. J., & Taylor, K. E. (2016). Overview of the coupled model intercomparison project phase 6 (CMIP6) experimental design and organization. *Geoscientific Model Development*, *9*(5), 1937–1958. https://doi.org/10.5194/gmd-9-1937-2016

Gelaro, R., McCarty, W., Suárez, M. J., Todling, R., Molod, A., Takacs, L., et al. (2017). The modern-era retrospective analysis for research and applications, version 2 (MERRA-2). *Journal of Climate*, *30*(14), 5419–5454. https://doi.org/10.1175/jcli-d-16-0758.1

Gertler, C. G., & O'Gorman, P. A. (2019). Changing available energy for extratropical cyclones and associated convection in Northern Hemisphere summer. *Proceedings of the National Academy of Sciences* (Vol. 116(10), 4105–4110). https://doi.org/10.1073/pnas.1812312116

Gertler, C. G., O'Gorman, P. A., Kravitz, B., Moore, J. C., Phipps, S. J., & Watanabe, S. (2020). Weakening of the extratropical storm tracks in solar geoengineering scenarios. *Geophysical Research Letters*, *47*(11), e2020GL087348. https://doi.org/10.1029/2020gl087348

Gidden, M. J., Riahi, K., Smith, S. J., Fujimori, S., Luderer, G., Kriegler, E., et al. (2019). Global emissions pathways under different socioeconomic scenarios for use in CMIP6: A dataset of harmonized emissions trajectories through the end of the century. *Geoscientific Model Development*, *12*(4), 1443–1475. https://doi.org/10.5194/gmd-12-1443-2019

Gillett, N. P., Shiogama, H., Funke, B., Hegerl, G., Knutti, R., Matthes, K., et al. (2016). The detection and attribution model intercomparison project (DAMIP v1. 0) contribution to CMIP6. *Geoscientific Model Development*, *9*(10), 3685–3697. https://doi.org/10.5194/gmd-9-3685-2016

Global Modeling and Assimilation Office (GMAO). (2015). MERRA-2 inst6_3d_ana_Np 3d,6-Hourly,Instantaneous,Pressure-Level,Analysis, Analyzed meteorological fields V5.12.4 [Dataset]. *Goddard Space Flight Center Distributed Active Archive Center (GSFC DAAC)*. https://doi.org/10.5067/A7S6XP56VZWS

Harvey, B., Cook, P., Shaffrey, L., & Schiemann, R. (2020). The response of the Northern Hemisphere storm tracks and jet streams to climate change in the CMIP3, CMIP5, and CMIP6 climate models. *Journal of Geophysical Research: Atmospheres*, *125*(23), e2020JD032701. https://doi.org/10.1029/2020jd032701

Henley, B. J., Gergis, J., Karoly, D. J., Power, S., Kennedy, J., & Folland, C. K. (2015). A tripole index for the interdecadal Pacific oscillation. *Climate Dynamics*, *45*(11–12), 3077–3090. https://doi.org/10.1007/s00382-015-2525-1

Hersbach, H., Bell, B., Berrisford, P., Biavati, G., Horányi, J. A., et al. (2023). ERA5 hourly data on pressure levels from 1940 to present [Dataset]. *Copernicus Climate Change Service (C3S) Climate Data Store (CDS)*. https://doi.org/10.24381/cds.bd0915c6

Hersbach, H., Bell, B., Berrisford, P., Hirahara, S., Horányi, A., Muñoz-Sabater, J., et al. (2020). The ERA5 global reanalysis. *Quarterly Journal of the Royal Meteorological Society*, *146*(730), 1999–2049. https://doi.org/10.1002/qj.3803

Hodnebrog, Ø., Myhre, G., Jouan, C., Andrews, T., Forster, P. M., Jia, H., et al. (2024). Recent reductions in aerosol emissions have increased Earth's energy imbalance. *Communications Earth & Environment*, *5*(1), 166. https://doi.org/10.1038/s43247-024-01324-8

Hoesly, R. M., Smith, S. J., Feng, L., Klimont, Z., Janssens-Maenhout, G., Pitkanen, T., et al. (2018). Historical (1750–2014) anthropogenic emissions of reactive gases and aerosols from the Community Emissions Data System (CEDS). *Geoscientific Model Development*, *11*(1), 369–408. https://doi.org/10.5194/gmd-11-369-2018

Hoskins, B., & Hodges, K. (2019). The annual cycle of northern hemisphere storm tracks. Part I: Seasons. *Journal of Climate*, *32*(6), 1743–1760. https://doi.org/10.1175/jcli-d-17-0870.1

Japan Meteorological Agency. (2023). Japanese reanalysis for three quarters of a century (JRA-3Q) [Dataset]. *Research Data Archive at the National Center for Atmospheric Research, Computational and Information Systems Laboratory*. Retrieved from https://rda.ucar.edu/datasets/d640000/

Kang, J. M. (2024). Data for Anthropogenic aerosols have significantly weakened the regional summertime circulation in the Northern Hemisphere during the satellite era [Dataset]. *Zenodo*. https://doi.org/10.5281/zenodo.11188121

Kang, J. M., Shaw, T. A., & Sun, L. (2023). Arctic sea ice loss weakens Northern Hemisphere summertime storminess but not until the late 21st century. *Geophysical Research Letters*, *50*(9), e2022GL102301. https://doi.org/10.1029/2022gl102301

Kang, S. M., Held, I. M., Frierson, D. M., & Zhao, M. (2008). The response of the ITCZ to extratropical thermal forcing: Idealized slab-ocean experiments with a GCM. *Journal of Climate*, *21*(14), 3521–3532. https://doi.org/10.1175/2007jcli2146.1

Kang, S. M., Xie, S.-P., Deser, C., & Xiang, B. (2021). Zonal mean and shift modes of historical climate response to evolving aerosol distribution. *Science Bulletin*, *66*(23), 2405–2411. https://doi.org/10.1016/j.scib.2021.07.013

Kaspi, Y., & Schneider, T. (2013). The role of stationary eddies in shaping midlatitude storm tracks. *Journal of the Atmospheric Sciences*, *70*(8), 2596–2613. https://doi.org/10.1175/jas-d-12-082.1

Klimont, Z., Smith, S. J., & Cofala, J. (2013). The last decade of global anthropogenic sulfur dioxide: 2000–2011 emissions. *Environmental Research Letters*, *8*(1), 014003. https://doi.org/10.1088/1748-9326/8/1/014003

Kosaka, Y., Kobayashi, S., Harada, Y., Kobayashi, C., Naoe, H., Yoshimoto, K., et al. (2024). The JRA-3Q reanalysis. *Journal of the Meteorological Society of Japan. Ser. II*, *102*(1), 49–109. https://doi.org/10.2151/jmsj.2024-004

Lehmann, J., & Coumou, D. (2015). The influence of mid-latitude storm tracks on hot, cold, dry and wet extremes. *Scientific Reports*, *5*(1), 1–9. https://doi.org/10.1038/srep17491

Leibensperger, E. M., Mickley, L. J., & Jacob, D. J. (2008). Sensitivity of US air quality to mid-latitude cyclone frequency and implications of 1980–2006 climate change. *Atmospheric Chemistry and Physics*, *8*(23), 7075–7086. https://doi.org/10.5194/acp-8-7075-2008

Martens, B., Schumacher, D. L., Wouters, H., Muñoz-Sabater, J., Verhoest, N. E., & Miralles, D. G. (2020). Evaluating the land-surface energy partitioning in ERA5. *Geoscientific Model Development*, *13*(9), 4159–4181. https://doi.org/10.5194/gmd-13-4159-2020

Mayer, J., Mayer, M., & Haimberger, L. (2021). Consistency and homogeneity of atmospheric energy, moisture, and mass budgets in ERA5. *Journal of Climate*, *34*(10), 3955–3974. https://doi.org/10.1175/jcli-d-20-0676.1

Ming, Y., & Ramaswamy, V. (2009). Nonlinear climate and hydrological responses to aerosol effects. *Journal of Climate*, *22*(6), 1329–1339. https://doi.org/10.1175/2008jcli2362.1

Ming, Y., Ramaswamy, V., & Chen, G. (2011). A model investigation of aerosol-induced changes in boreal winter extratropical circulation. *Journal of Climate*, *24*(23), 6077–6091. https://doi.org/10.1175/2011jcli4111.1

Needham, M. R., & Randall, D. A. (2023). Anomalous northward energy transport due to anthropogenic aerosols during the twentieth century. *Journal of Climate*, *36*(19), 6713–6728. https://doi.org/10.1175/jcli-d-22-0798.1

O'Gorman, P. A. (2010). Understanding the varied response of the extratropical storm tracks to climate change. *Proceedings of the National Academy of Sciences*, *107*(45), 19176–19180. https://doi.org/10.1073/pnas.1011547107

Persad, G. G., Samset, B. H., & Wilcox, L. J. (2022). Aerosols must be included in climate risk assessments. *Nature*, *611*(7937), 662–664. https://doi.org/10.1038/d41586-022-03763-9

Pfleiderer, P., Schleussner, C.-F., Kornhuber, K., & Coumou, D. (2019). Summer weather becomes more persistent in a 2° C world. *Nature Climate Change*, *9*(9), 666–671. https://doi.org/10.1038/s41558-019-0555-0

Quaas, J., Jia, H., Smith, C., Albright, A. L., Aas, W., Bellouin, N., et al. (2022). Robust evidence for reversal of the trend in aerosol effective climate forcing. *Atmospheric Chemistry and Physics*, *22*(18), 12221–12239. https://doi.org/10.5194/acp-22-12221-2022

Saha, S., Moorthi, S., Pan, H.-L., Wu, X., Wang, J., Nadiga, S., et al. (2010). NCEP climate forecast system reanalysis (CFSR) 6-hourly products, January 1979 to december 2010 [Dataset]. *Research Data Archive at the National Center for Atmospheric Research, Computational and Information Systems Laboratory*. Retrieved from https://rda.ucar.edu/datasets/d093000/

Saha, S., Moorthi, S., Pan, H.-L., Wu, X., Wang, J., Nadiga, S., et al. (2010). The NCEP climate forecast system reanalysis. *Bulletin of the American Meteorological Society*, *91*(8), 1015–1058. https://doi.org/10.1175/2010bams3001.1

Saha, S., Moorthi, S., Wu, X., Wang, J., Nadiga, S., Tripp, P., et al. (2011). NCEP climate forecast system version 2 (CFSv2) 6-hourly products [Dataset]. *Research Data Archive at the National Center for Atmospheric Research, Computational and Information Systems Laboratory*. Retrieved from https://rda.ucar.edu/datasets/d094000/

Saha, S., Moorthi, S., Wu, X., Wang, J., Nadiga, S., Tripp, P., et al. (2014). The NCEP climate forecast system version 2. *Journal of Climate*, *27*(6), 2185–2208. https://doi.org/10.1175/jcli-d-12-00823.1

Sardeshmukh, P. D., & Hoskins, B. I. (1984). Spatial smoothing on the sphere. *Monthly Weather Review*, *112*(12), 2524–2529. https://doi.org/10.1175/1520-0493(1984)112<2524:ssots>2.0.co;2

Schmidt, G. (2013). On mismatches between models and observations. https://www.realclimate.org/index.php/archives/2013/09/on-mismatches-between-models-and-observations/

Schumacher, D. L., Singh, J., Hauser, M., Fischer, E. M., Wild, M., & Seneviratne, S. I. (2024). Exacerbated summer European warming not captured by climate models neglecting long-term aerosol changes. *Communications Earth & Environment*, *5*(1), 182. https://doi.org/10.1038/s43247-024-01332-8

Shaw, T. A., Barpanda, P., & Donohoe, A. (2018). A moist static energy framework for zonal-mean storm-track intensity. *Journal of the Atmospheric Sciences*, *75*(6), 1979–1994. https://doi.org/10.1175/jas-d-17-0183.1

Shaw, T. A., Miyawaki, O., & Donohoe, A. (2022). Stormier Southern Hemisphere induced by topography and ocean circulation. *Proceedings of the National Academy of Sciences* (Vol. 119(50), e2123512119). https://doi.org/10.1073/pnas.2123512119

Shaw, T. A., & Smith, Z. (2022). The midlatitude response to polar sea ice loss: Idealized slab-ocean aquaplanet experiments with thermodynamic sea ice. *Journal of Climate*, *35*(8), 2633–2649. https://doi.org/10.1175/jcli-d-21-0508.1

Shaw, T. A., & Voigt, A. (2015). Tug of war on summertime circulation between radiative forcing and sea surface warming. *Nature Geoscience*, *8*(7), 560–566. https://doi.org/10.1038/ngeo2449

Shaw, T. A., & Voigt, A. (2016). Land dominates the regional response to CO2 direct radiative forcing. *Geophysical Research Letters*, *43*(21), 11–383. https://doi.org/10.1002/2016gl071368

Shen, Z., & Ming, Y. (2018). The influence of aerosol absorption on the extratropical circulation. *Journal of Climate*, *31*(15), 5961–5975. https://doi.org/10.1175/jcli-d-17-0839.1

Undorf, S., Bollasina, M., & Hegerl, G. (2018). Impacts of the 1900–74 increase in anthropogenic aerosol emissions from North America and Europe on Eurasian summer climate. *Journal of Climate*, *31*(20), 8381–8399. https://doi.org/10.1175/jcli-d-17-0850.1

Wang, Y., Jiang, J. H., & Su, H. (2015). Atmospheric responses to the redistribution of anthropogenic aerosols. *Journal of Geophysical Research: Atmospheres*, *120*(18), 9625–9641. https://doi.org/10.1002/2015jd023665

Wang, Y., Wang, M., Zhang, R., Ghan, S. J., Lin, Y., Hu, J., et al. (2014). Assessing the effects of anthropogenic aerosols on Pacific storm track using a multiscale global climate model. *Proceedings of the National Academy of Sciences* (Vol. 111(19), 6894–6899). https://doi.org/10.1073/pnas.1403364111

Wang, Z., Lin, L., Xu, Y., Che, H., Zhang, X., Zhang, H., et al. (2021). Incorrect Asian aerosols affecting the attribution and projection of regional climate change in CMIP6 models. *npj Climate and Atmospheric Science*, *4*(1), 2. https://doi.org/10.1038/s41612-020-00159-2

Xie, S.-P., Lu, B., & Xiang, B. (2013). Similar spatial patterns of climate responses to aerosol and greenhouse gas changes. *Nature Geoscience*, *6*(10), 828–832. https://doi.org/10.1038/ngeo1931

Zhang, R., Li, G., Fan, J., Wu, D. L., & Molina, M. J. (2007). Intensification of Pacific storm track linked to Asian pollution. *Proceedings of the National Academy of Sciences* (Vol. 104(13), 5295–5299). https://doi.org/10.1073/pnas.0700618104

Zhang, Y., Li, Y., Guo, J., Wang, Y., Chen, D., & Chen, H. (2019). The climatology and trend of black carbon in China from 12-year ground observations. *Climate Dynamics*, *53*(9–10), 5881–5892. https://doi.org/10.1007/s00382-019-04903-0